Development and validation of a Kalman filter based load torque estimation method for electric axle drives

Robert Kalcher*

AMSD Advanced Mechatronic System Development KG,
Reininghausstrasse 13a, 8020 Graz, Austria
Email: robert.kalcher@amsd.at
*Corresponding author

Katrin Ellermann

Institute of Mechanics,
Graz University of Technology,
Kopernikusgasse 24/IV, 8010 Graz, Austria
Email: ellermann@tugraz.at

Gerald Kelz

AMSD Advanced Mechatronic System Development KG,
Reininghausstrasse 13a, 8020 Graz, Austria
Email: kelz@amsd.at

Karl Heinz Reisinger

Institute of Automotive Engineering,
FH Joanneum Graz University of Applied Sciences,
Alte Poststrasse 149, 8020 Graz, Austria
Email: karlheinz.reisinger@fh-joanneum.at

Abstract: Based on the automotive development strategies towards electrification and autonomous driving, the need of enhancements regarding state estimations, extended diagnosis as well as redundant architectures are evident. Accurate, robust and cost-efficient load torque estimation methods can bring significant benefits in this respect. Thus, this work presents a Kalman filter based load torque estimation method for electric axle drives by mean of virtual sensing. The elastically mounted electric rear axle drive of a Renault Twizy 80 was installed at a powertrain test rig. Using the measurement results, the parameters of a multi-body system (MBS) model were adjusted, in order to obtain a reference model for method validation. Subsequently, the basic functioning of the proposed load torque estimation method was shown by several test manoeuvres based on the measurement-adjusted reference model. The investigations revealed favourable results even in the case of reasonable effective torque dynamics (up to 3 Hz) and realistic sensor noise.

Keywords: load torque estimation; electric rear axle drives; ERAD; electric rear axle drive; virtual sensing; Kalman filter; multi-body systems; multi-body simulations; MBS; multi-body system; powertrain test rig; simulation–measurement adjustment.

Reference to this paper should be made as follows: Kalcher, R., Ellermann, K., Kelz, G. and Reisinger, K.H. (2023) ‘Development and validation of a Kalman filter based load torque estimation method for electric axle drives’, *Int. J. Vehicle Performance*, Vol. 9, No. 1, pp.41–72.

Biographical notes: Robert Kalcher is PhD student at the Institute of Mechanics, Faculty of Mechanical Engineering and Economic Sciences at Graz University of Technology. He received his BSc and his MSc in Civil Engineering from Graz University of Technology in 2009 and 2013, respectively. Furthermore, he received a diploma degree in Automotive Engineering from the University of Applied Sciences FH Joanneum Graz in 2014. He is currently employed at AMSD Advanced Mechatronic System Development KG as development and simulation engineer for the automotive sector. His research interests include non-linear dynamics and multi-body systems.

Katrin Ellermann holds a MSc in Mechanical Engineering from Hamburg University of Technology and a Master of Engineering from the Cornell University. She received her PhD in Mechanical Engineering from Hamburg University of Technology in 2002. She worked as researcher at Hamburg University of Technology and at the University of California, Berkeley. In 2010, she was appointed as Professor for the Institute of Mechanics at Graz University of Technology. Her research interests include non-linear and stochastic dynamics, multi-body systems and structural vibrations.

Gerald Kelz holds MSc in Mechanical Engineering as well as Industrial Engineering and Management from Graz University of Technology. Moreover, he received his PhD in Mechanical Engineering from Graz University of Technology in 2010. He began his professional career as researcher at the Institute of Mechanics and, subsequently, at the Institute of Automotive Engineering, both at Graz University of Technology. In 2010, he founded the engineering company AMSD Advanced Mechatronic System Development KG, at which he is currently executive manager. His research interests include non-linear dynamics, multi-body systems and powertrain simulations.

Karl Heinz Reisinger holds a MSc in Mechanical Engineering and received his PhD in Mechanical Engineering from Graz University of Technology in 1999. He started his professional career at Magna Steyr in 1999. From 2003 to 2007 he was responsible for the department *Actuatorics and Functional Software Development*. Since 2007 he is at the Institute of Automotive Engineering at FH Joanneum Graz University of Applied Sciences in the position of an Associated Professor.

1 Introduction

The observation of the changes within the fleets of renowned vehicle manufacturers reveal that the number of electric vehicles – especially battery electric vehicles (BEVs) – increased steadily in recent time, see for instance Gavric (2020). Here, in particular BEVs with electric drives on the front axle (i.e., electric front axle drive, EFAD) and / or on the rear axle (i.e., electric rear axle drive, ERAD) – are frequently deployed, cf. Hauptmann (2018) and Doerr et al. (2018). A few examples of such production vehicles with electric axle drives are: *Tesla Model 3/S/X/Y*, *BMW iX3*, *VW ID.3/ID.4*, *Audi e-tron*, *Mercedes-Benz EQA/EQC* and in the microcar segment the *Renault Twizy*. Additionally to this development strategy towards electrification, autonomous driving and advanced driver assistance systems (ADAS) also play an increasingly important role in the field of automotive engineering. Both trends highlight the need of enhancements within the following topics regarding electrified powertrains:

- state estimations for control applications
- diagnosis and fault detection as well as
- redundant architecture for fail-operational systems.

Accurate, robust and cost-efficient estimation methods for the load torque at the drive shafts can bring significant benefits in this respect. This should be discussed in detail below.

First, for vehicle dynamics control systems – such as electronic stability control (ESC) –, tyre–road friction (TRF) estimators are of crucial importance, see Reif (2011). Here, the wheel torques represent an essential input quantity for these TRF estimators. In general, the wheel torques can be approximately calculated via the motor torque, associated gear ratios and drivetrain efficiency factors. But a sophisticated load torque determination and subsequently a more precise wheel torque calculation would entail a clear potential for improvement, cf. Lex (2015).

Furthermore, a comparison of the motor torque and the load torque of an electric axle drive would facilitate an enhanced drivetrain diagnosis. By evaluating the differences of these two torque signals, losses within the drivetrain (e.g., gear meshing losses) can be observed and even mechanical faults (e.g., grinding parts or intrusion of oil into motor's air gap) can be detected. It is obvious that this would provide a valuable insight into the operating state.

On the other hand, safety-critical applications, for example in the field of autonomous driving, require a sufficiently independent redundancy in order to provide a fail-operational behaviour, see Schnellbach et al. (2016). Although the motor torque of an electric axle drive can be estimated on the basis of the measured phase current, another independent torque calculation principle would be beneficial for an increased redundancy level.

This work presents a novel model-based load torque estimation technique using Kalman filtering. The underlying basic principle uses the fact that vehicle drivetrain components, such as transfer cases or electric axle drives, are usually mounted to the structure (e.g., chassis, subframe, etc.) via flexible elastomer mounts (or also called rubber bushings), see for example Lennström (2015). Based on a torque transfer during operation, a specific drivetrain component thus twists in relation to the structure. This relative twist motion is influenced by the transferred torque, the inertia of the component as also the positions, stiffness and damping characteristics of the elastomer mounts. Hence, it is evident that the transferred torque can be observed on basis of measured drivetrain component twist motions. Even in the case of mass-produced vehicles, these twist motions can be easily measured through the application of standard automotive angle sensors, well-known from throttle, pedal or steering wheel angular position sensors.

It should be emphasised that the whole motion of an elastically mounted drivetrain component can be determined by only one angle sensor for the component's rotation axis, which is commonly referred to as torque roll axis (TRA), see for instance Courteille et al. (2005). In the proposed method, a Kalman filter combines these available measurements and the a priori knowledge of the system – defined by an appropriate filter model – for an optimal estimation of the load torque. In more detail, the filter model consists of a simple single-degree-of-freedom (SDOF) torsional oscillator, as representation of the inertia of the drivetrain component, in conjunction with a torsional spring–damper for a lumped modelling of all contributing elastomer mounts. This approach of using easily available measurements in combination with numerical models of the system in order to estimate another quantity indirectly is often referred to as 'virtual sensing', see Prokhorov (2005), Forrier (2018) and Risaliti et al. (2019).

In general, a survey of literature reveal that torque estimators using Kalman filters and observers are widely used in both, automotive and also industrial applications. In Forrier et al. (2017), a broadband virtual torque sensor was developed for a generic mechatronic powertrain. For this purpose, augmented non-linear Kalman filters based on electrical and mechanical models were applied. The stator current phasor of the induction motor, the rotor angle and rotational velocities or accelerations at motor as also load side depict the necessary measurement signals. In Schaper et al. (2009), a mechanical dual mass flywheel (DMF) model was deployed for an observer-based torque estimation at low engine speeds. For this method, the angular velocities at both DMF sides as also the displacement angle of the DMF were used as measurements. In Kiencke (1999), a Kalman filter for the estimation of the combustion torque of reciprocating engines was presented. In this approach, only sensor signals commonly available in engine management systems – such as engine speed and top dead centre (TDC) information – were used. In Khiar et al. (2005), a similar principle was deployed for an observer-based estimation of the instantaneous torque of internal combustion engines (ICEs). Moreover, the works (Chauvin et al., 2004; Helm et al., 2012; Jakubek and Fleck, 2009) should be mentioned, where the inner torque of ICEs at engine test rigs was estimated via Kalman filtering techniques. In contrast to these torque estimations, the basic principle of the method proposed in this work is substantially different. Since it is based on the elastic mounting of drive units and the corresponding motion with respect to the structure. Therefore, the proposed load torque estimation method features a significant degree of novelty and hence promising application potentials in the field of modern electrified automotive powertrains.

For a detailed examination of the possible field of application of the proposed load torque estimation method, the basic powertrain topologies for electrified vehicles should be analysed in more detail, see Figure 1 (cf. Hofmann (2014)).

The left hand side of Figure 1 visualises the concepts which are out of scope of the proposed load torque estimation method, namely: wheel hub and close-to-wheel drives. These two concepts show great potentials regarding efficiency and installation space, but suffers from drawbacks relating to an increased unsprung mass as also to an additional technical effort, see Tschoeke et al. (2019), Kasper and Schünemann (2012) and Wallentowitz and Freialdenhoven (2011).

Figure 1 Basic powertrain topologies for electrified vehicles, cf. Hofmann (2014) (see online version for colours)

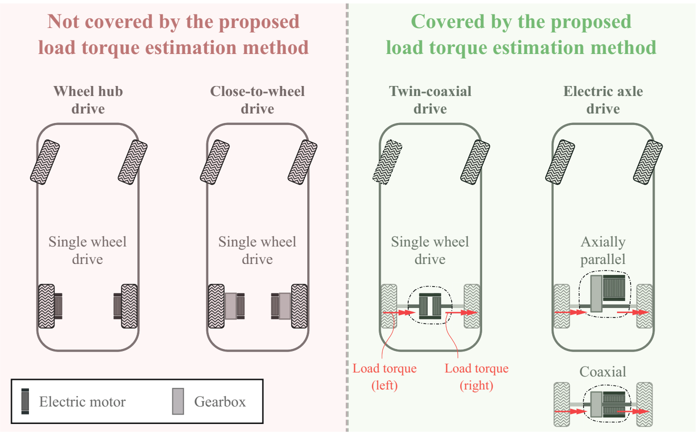

The right hand side of Figure 1 shows the so-called *central motor concepts*, on which the proposed load torque estimation method can be applied. It can be seen that the possible field of application is not limited to electric axle drives (both axially parallel and coaxial design), but can also be applied to twin-coaxial drives. Furthermore, the load torques to be determined by the proposed estimation method are depict. Here, the load torques are composed of the left and right hand side parts acting on the corresponding side shafts.

A survey of the current market of mass-produced BEVs reveal the dominant role of central motor concepts and here especially electric axle drives, see also Eghtessad et al. (2015). This can be highlighted by well-documented development examples of car manufacturers (Doerr et al., 2020; Siebenpfeiffer, 2015) and by automotive suppliers Höfer et al. (2020), Mühlberg et al. (2017), Smetana et al. (2013) and Domian et al. (2013). Especially in Lieske et al. (2020) the importance of the elastic mounting of electric drive units was emphasised. Therefore, it can be concluded that the field of application of the proposed load torque estimation method covers a great amount of electrified powertrains within BEVs and also axle-split hybrid electric vehicles (HEVs).

In Kalcher et al. (2022), the novel model-based load torque estimation method using Kalman filtering was extensively presented. There, it was focused on the modelling of the elastomer mounts and especially the implications of the non-linear effect of static hysteresis. As the method verification there was limited to a numerical validation with aid of multi-body system (MBS) simulations, the work at hand goes one step further and provides a hybrid experimental–numerical validation procedure, cf. Zeller (2018). Here, a sophisticated MBS simulation model is adjusted on basis of real-world powertrain test rig measurements of the ERAD of a *Renault Twizy 80*.

This paper is structured as follows. Section 2 introduces the load torque estimation principle, namely, the filter model as also the associated Kalman filter framework. Section 3 deals with the measurement configuration used. Here, the test rig set-up with the associated sensors are presented. Moreover, a so-called *test plan* is introduced on basis of a list of test manoeuvres to be carried out. In Section 4, the measurement outputs are described. Particularly, the simulation–measurement adjustment process and the corresponding parameter identification for the MBS simulation model are depicted.

Section 5 presents the method validation on basis of the measurement-adjusted MBS simulation model. Here, several load torque estimations are comprehensively evaluated. Additionally, the proposed load torque estimation method is analysed using influence analyses. Finally, the paper concludes with a summary and a short outlook on future improvements.

2 Load torque estimation

Usually, the electric axle drive of a BEV is mounted elastically to the chassis (or subframe) via rubber sleeve bushings, see Roth et al. (2019). Here, various configurations are used, cf. Schwartz (2014):

- three point mounting layout
- four point mounting layout
- three point pendulum concept with roll restrictor.

These basic configurations are visualised in Figure 2 using the example of an ERAD. As the names imply, the three and four point mounting layouts consist of three and four rubber sleeve bushings, respectively. Where the design with four bushings is the more expensive solution but has the advantage of lower mount forces. In contrast to these two layouts, the three point pendulum concept deploys two mounts, which are approximately positioned at the TRA and an additional roll restrictor. The main purposes of the two mounts are to carry the weight of the electric axle drive and also to restrict vertical, lateral and longitudinal travels. On the other hand, the roll restrictor mainly controls the movements due to load torques. This task separation allows a good tuning of characteristics but – in comparison to the other two layouts – the design freedom is more restricted.

Figure 2 Basic mounting configurations of electric axle drives (see online version for colours)

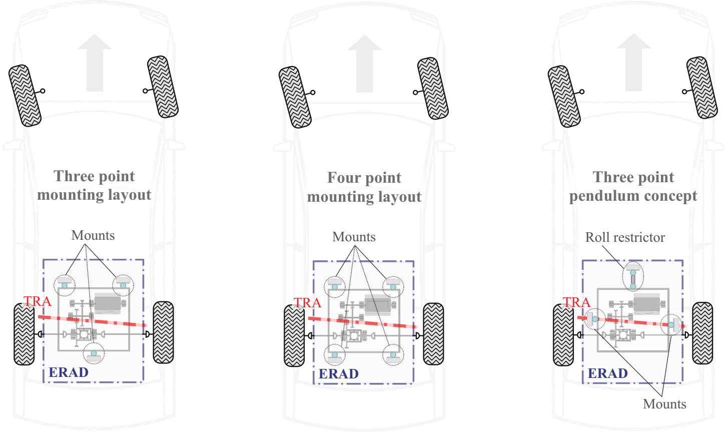

Since the Renault Twizy – which is under consideration here – has a three point mounting layout, the following derivations in this section refer to this configuration. The proposed Kalman filter based load torque estimation method can be easily transferred to any other elastic mounting concept. With this in mind, the Kalman filter model can be derived.

2.1 Filter model

For the elastically mounted – and otherwise unconstrained – Twizy ERAD with mass m and inertia tensor $\boldsymbol{I}$, an acting time-dependent load torque vector $\boldsymbol{T}_\mathrm{l}(t)$ along the drive shaft axis entails almost solely a twist about the uniquely determinable TRA, see left hand side of Figure 3. Here, the rubber bushings in the points B_i $(i = 1, \ldots, 3)$ are depicted with help of the elastomer mount forces $\boldsymbol{F}_i$ and the corresponding position vectors $\boldsymbol{r}_i$. Whereby the position vectors are with respect to A, which is an arbitrary defined point on the TRA. Consequently, as Kalman filter model, a simple SDOF torsional oscillator is used, see right hand side of Figure 3. Here, a rigid body with a mass moment of inertia I is connected to a fixed environment via a revolute joint about the TRA. Furthermore, the TRA-projected restoring torque of the elastomer mount forces $T_\mathrm{e}(\mathbf{x}(t))$ is generally represented by a torsional bushing. The TRA is depicted with the unit direction vector $\boldsymbol{e}_\mathrm{TRA}$. It can be clearly seen that the TRA in the right hand side of Figure 3 is in projected display and thus the unit direction vector $\boldsymbol{e}_\mathrm{TRA}$ truncates to a point in A. The twist angle $\phi(t)$ about the TRA exhibits the only degree of freedom (DOF) of the model. Thus, the twist angle and its time derivative, the twist angle velocity $\dot{\phi}(t)$, yield the state variables of the filter model:

$$\mathbf{x}(t) = \begin{bmatrix} \phi(t) \\ \dot{\phi}(t) \end{bmatrix}. \tag{1}$$

Thus, the equation of motion for the Kalman filter model reads:

$$\ddot{\phi}(t) = \frac{1}{I} \cdot \Big(T_\mathrm{l}(t) + T_\mathrm{e}(\mathbf{x}(t)) \Big), \tag{2}$$

where $\ddot{\phi}(t)$ stands for the twist angle acceleration, $T_\mathrm{e}(\mathbf{x}(t))$ denotes the TRA-projected torque of the elastomer mount forces

$$T_\mathrm{e}(\mathbf{x}(t)) = \boldsymbol{e}_\mathrm{TRA} \cdot \left(\sum_{i=1}^{3} \boldsymbol{r}_i \times \boldsymbol{F}_i(\mathbf{x}(t)) \right), \tag{3}$$

and

$$T_\mathrm{l}(t) = \boldsymbol{e}_\mathrm{TRA} \cdot \boldsymbol{T}_\mathrm{l}(t), \tag{4}$$

designates the TRA-projected part of the load torque vector. Due to the unique conversion in equation (4), in the following only the scalar-valued time history $T_\mathrm{l}(t)$ needs to be determined with aid of the proposed load torque estimation method. Furthermore, it should be mentioned here that the filter model derivation is carried out in static equilibrium state and hence no weight forces have to be considered.

For the further derivation of the torsional bushing, the elastomer mounts of the Twizy have to be examined in more detail. In all three mounting points, typical rubber sleeve bushings are installed, which are basically constructed as shown in the left hand side of Figure 4. An outer metal sleeve is coupled via rubber to an inner metal sleeve. Optional pockets within the elastomer facilitate the adjustment of a desired non-linear stiffness behaviour. A typical quasi-static force–displacement characteristic curve in radial direction is visualised in the right hand side of Figure 4. In most cases, a clear linear domain around the origin can be identified, where the associated force law is described by a nearly constant spring stiffness. Radial mount displacements exceeding this linear domain entail a noticeable stiffening, which in turn results in a progressive force–displacement curve. The reasons for this typical progression domain in radial direction are – at the beginning – the closing of possibly existing pockets and further on, the blocking of the inner and outer metal sleeves to each other. On the other hand, in axial direction the stiffness is approximately constant in a wide range and a clear progression domain can only be implemented with help of additional limit stops.

Figure 3 Elastically mounted Twizy ERAD with displayed TRA (left hand side) and associated SDOF torsional oscillator filter model (right hand side) (see online version for colours)

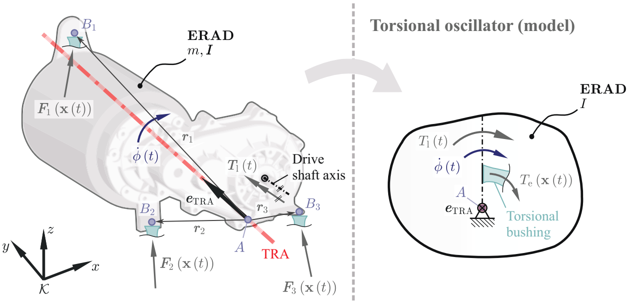

Figure 4 Typical rubber sleeve bushing and its quasi-static behaviour in radial direction (see online version for colours)

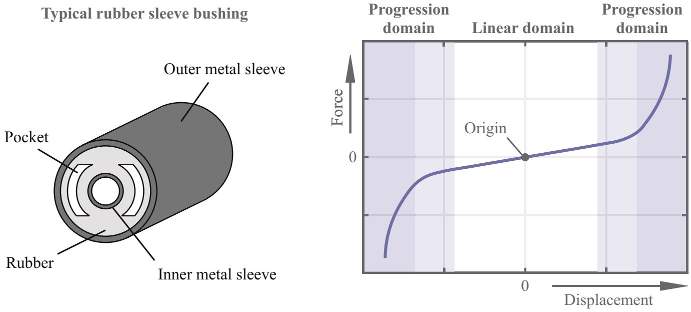

This behaviour described can be confirmed by real measurements of the Twizy elastomer mounts. Figure 5 shows the rubber bushing test set-up as well as the measured quasi-static characteristic curves of force F against rubber mount displacement s. In the upper part of Figure 5, the measurement results of the axial direction of the rubber bushing in B_3 is visualised. Moreover, in the lower part of Figure 5, the measurement results of the radial direction of the rubber bushing in B_2 is displayed. The axial direction shows an approximately linear relationship between force and displacement. Whereas for the radial direction, the beginning of the progression based on the metal sleeve blocking become apparent for a displacement over 2 mm. The evaluation of the rubber mount displacements during a typical Twizy ERAD operation on the powertrain test rig revealed that even the radial bushing displacements are limited to the linear domain.

Figure 5 Quasi-static measurements for two Twizy elastomer mounts: (a) measurement results of the axial direction of the rubber bushing in B_3 and (b) measurement results of the radial direction of the rubber bushing in B_2 (see online version for colours)

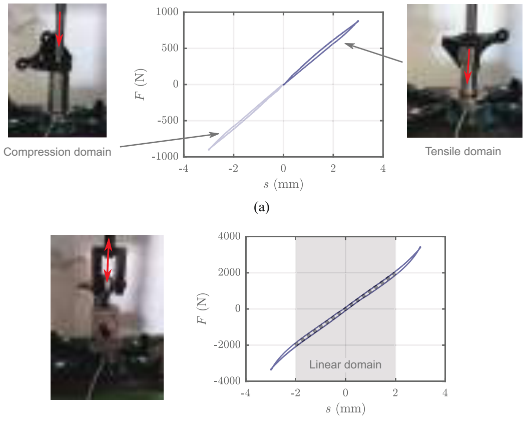

(a)

(b)

Furthermore, from the example measurements of the Twizy elastomer mounts it can be seen that the static hysteresis is negligibly small for both, the axial and the radial directions. Hence, a sophisticated modelling of friction and amplitude dependence – as in Kalcher et al. (2022) – is not necessary. Since the focus is also only on a load torque estimation method for the low frequency domain, no special rheological models are required to depict the dependence on the excitation frequency in more detail. Thus, it is sufficient to describe the elastic mounting of the Twizy ERAD within the filter model through a torsional Kelvin–Voigt element with constant parameters. Hence, the elastomer mount forces can be described with the stiffness tensors $\boldsymbol{K}_i$ and damping tensors $\boldsymbol{D}_i$ of all rubber bushings (assuming sufficiently small angles which allow for a linearisation):

$$\boldsymbol{F}_i\left(\mathbf{x}\left(t\right)\right) = -\left(\boldsymbol{K}_i \cdot \boldsymbol{l}_i\right) \cdot \phi\left(t\right) - \left(\boldsymbol{D}_i \cdot \boldsymbol{l}_i\right) \cdot \dot{\phi}\left(t\right), \tag{5}$$

where $\boldsymbol{l}_i = \boldsymbol{e}_{\mathrm{TRA}} \times \boldsymbol{r}_i$ designate the vectors for the calculation of the rubber bushing kinematics. The bushing-dependent stiffness and damping tensors can be expressed by the following diagonal matrices, see Park and Singh (2007):

$$\mathbf{K}_i = \begin{bmatrix} k_{i\,x} & 0 & 0 \\ & k_{i\,y} & 0 \\ \mathrm{sym.} & & k_{i\,z} \end{bmatrix}, \quad \mathbf{D}_i = \begin{bmatrix} d_{i\,x} & 0 & 0 \\ & d_{i\,y} & 0 \\ \mathrm{sym.} & & d_{i\,z} \end{bmatrix}. \tag{6}$$

This formulation takes the advantage that all three rubber sleeve bushings of the Twizy are aligned normal to each other and hence all matrices can be expressed in the global coordinate system $\mathcal{K}$ (see left hand side of Figure 3). Furthermore, only the translational compliances are considered, because for standard automotive rubber bushings, the rotational stiffnesses and dampings can be neglected, see for instance Jeong and Singh (2000) and Alkhatib (2013).

Thus, the restoring torque from equation (3) can be rewritten in the following way:

$$T_{\mathrm{e}}\left(\mathbf{x}\left(t\right)\right) = -\boldsymbol{e}_{\mathrm{TRA}} \cdot \left(\sum_{i=1}^{3} \boldsymbol{r}_i \times \Big(\left(\boldsymbol{K}_i \cdot \boldsymbol{l}_i\right) \cdot \phi\left(t\right) + \left(\boldsymbol{D}_i \cdot \boldsymbol{l}_i\right) \cdot \dot{\phi}\left(t\right)\Big)\right). \tag{7}$$

Using equation (7), the torsional spring stiffness as well as the torsional damping factor can be identified:

$$\begin{aligned} k_{\phi} &= \boldsymbol{e}_{\mathrm{TRA}} \cdot \left(\sum_{i=1}^{3} \boldsymbol{r}_i \times \left(\boldsymbol{K}_i \cdot \boldsymbol{l}_i \right) \right), \\ d_{\phi} &= \boldsymbol{e}_{\mathrm{TRA}} \cdot \left(\sum_{i=1}^{3} \boldsymbol{r}_i \times \left(\boldsymbol{D}_i \cdot \boldsymbol{l}_i \right) \right). \end{aligned} \tag{8}$$

Finally, the equation of motion for the Kalman filter model from equation (2) can be rewritten in the following way:

$$\ddot{\phi}\left(t\right) = \frac{1}{I} \cdot \Big(T_{\mathrm{l}}\left(t\right) - k_{\phi} \cdot \phi\left(t\right) - d_{\phi} \cdot \dot{\phi}\left(t\right) \Big), \tag{9}$$

which facilitates a planar description of the generally three-dimensional ERAD movement.

Furthermore, it should be noted that equation (9) represents a fully linear model. Therefore, the torque estimation can be performed with a simple Kalman filter and the associated non-linear versions such as extended Kalman filter (EKF; see Simon (2006)) and unscented Kalman filter (UKF; cf. Julier et al. (1995) and Julier and Uhlmann (2004)) do not have to be applied. For detailed information regarding the consideration of non-linear effects (e.g., progression and static hysteresis) and hence the application of an UKF as a non-linear torque estimator, please refer to Kalcher et al. (2022).

2.2 *Kalman filter framework*

In this section, the Kalman filter framework for the proposed model-based load torque estimation method is presented, cf. Kalcher et al. (2022). Here, the so-called virtual torque sensor principle is used in order to estimate the load torque of the Twizy ERAD at the powertrain test rig on basis of easily available measurements, such as the twist motions about the TRA. In Figure 6, the principle of the virtual torque sensor is visualised in flow chart form. The Twizy ERAD at the powertrain test rig depicts the observed system. The accelerator pedal value of the electric motor α_{p} and the rotational speeds of both dynos (i.e.: left hand side: $n_{\mathrm{l}}\left(t\right)$; right hand side: $n_{\mathrm{r}}\left(t\right)$) define the load torque to be estimated. Moreover, the output of the system is described by the state variables of the filter model, that is to say, the twist angle about the TRA and its time derivative. If the time derivative of the twist angle is not available by measurements, it can always recursively be calculated based on the twist angle via numerical differentiation. As in real measurements, sensor noise is always present, it also has to be considered for the input of the virtual sensor. The virtual sensor is represented by a Kalman filter, which in turn comprises of two stages. First, the prediction is done with help of the filter model and, second, the estimator performs a correction on basis of the current measurements. After that, the Kalman filter outputs the estimated load torque for the corresponding time step.

Figure 6 Kalman filter framework for the proposed model-based load torque estimation method (see online version for colours)

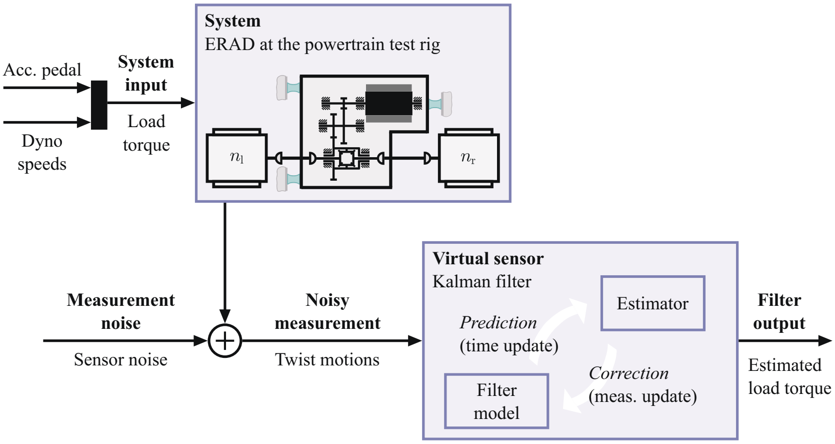

For the application of the virtual sensor principle, first, the ERAD at the powertrain test rig was formulated as so-called *augmented* state-space system. Here, not only the original states of the filter model have to be considered within the column matrix of the state variables, but also the unknown input, that is to say, the load torque, cf. Lourens et al. (2012), Naets et al. (2014) and Ray (1997):

$$\bar{\mathbf{x}}(t) = \begin{bmatrix} \phi(t) \\ \dot{\phi}(t) \\ T_\mathrm{l}(t) \end{bmatrix} . \tag{10}$$

For the corresponding state equation of the load torque, a zero$^{\mathrm{th}}$-order random walk model is applied, see Naets et al. (2015a) and Cumbo et al. (2019), but other models are also conceivable, cf. Ray (1995):

$$\dot{T}_\mathrm{l}(t) = w_T(t) , \tag{11}$$

where $w_T(t)$ designates the load torque process noise. Thus, the state equations of the augmented system yield:

$$\underbrace{\begin{bmatrix} \dot{\phi}(t) \\ \ddot{\phi}(t) \\ \dot{T}_\mathrm{l}(t) \end{bmatrix}}_{=:\dot{\bar{\mathbf{x}}}(t)} = \underbrace{\begin{bmatrix} 0 & 1 & 0 \\ -\frac{k_\phi}{I} & -\frac{d_\phi}{I} & 1 \\ 0 & 0 & 0 \end{bmatrix}}_{=:\bar{\mathbf{A}}} \cdot \underbrace{\begin{bmatrix} \phi(t) \\ \dot{\phi}(t) \\ T_\mathrm{l}(t) \end{bmatrix}}_{=\bar{\mathbf{x}}(t)} + \underbrace{\begin{bmatrix} 0 \\ 0 \\ w_T(t) \end{bmatrix}}_{=:\mathbf{w}(t)} , \tag{12a}$$

$$\dot{\bar{\mathbf{x}}}(t) = \bar{\mathbf{A}} \cdot \bar{\mathbf{x}}(t) + \mathbf{w}(t) , \tag{12b}$$

where $\dot{\bar{\mathbf{x}}}(t)$ is the column matrix with the time derivatives of the states of the augmented system and $\mathbf{w}(t)$ denotes the column matrix of the process noise. Moreover, the associated output equations read:

$$\underbrace{\begin{bmatrix}\phi(t)\\ \dot{\phi}(t)\end{bmatrix}}_{=\mathbf{y}(t)} = \underbrace{\begin{bmatrix}1\,0\,0\\ 0\,1\,0\end{bmatrix}}_{=:\bar{\mathbf{C}}} \cdot \underbrace{\begin{bmatrix}\phi(t)\\ \dot{\phi}(t)\\ T_{\mathrm{l}}(t)\end{bmatrix}}_{=\bar{\mathbf{x}}(t)} + \underbrace{\begin{bmatrix}v_{\phi}(t)\\ v_{\dot{\phi}}(t)\end{bmatrix}}_{=\mathbf{v}(t)}, \tag{13a}$$

$$\mathbf{y}(t) = \bar{\mathbf{C}} \cdot \bar{\mathbf{x}}(t) + \mathbf{v}(t), \tag{13b}$$

where $\mathbf{v}(t)$ designates the column matrix for the sensor noise, which consists of the measurement noise for the twist angle $v_{\phi}(t)$ and the twist angle velocity $v_{\dot{\phi}}(t)$, respectively. Furthermore, the state matrix and the output matrix of the augmented system are designated by $\bar{\mathbf{A}}$ and $\bar{\mathbf{C}}$, respectively.

Using standard discretisation schemes (see for instance Maes et al. (2019), Risaliti et al. (2016), Bachinger et al. (2014)), the discrete-time state-space representation of the augmented system can be formulated as follows:

$$\bar{\mathbf{x}}_k = \mathbf{\Phi} \cdot \bar{\mathbf{x}}_{k-1} + \mathbf{w}_{k-1}, \tag{14a}$$

$$\mathbf{y}_{k-1} = \bar{\mathbf{C}} \cdot \bar{\mathbf{x}}_{k-1} + \mathbf{v}_{k-1}, \tag{14b}$$

where $\mathbf{\Phi}$ is the state transition matrix, that is to say, the time-discretised representation of the continuous-time state matrix $\bar{\mathbf{A}}$ of the augmented system from equation (12). The indices k and $k-1$ stand for time instants, which are described by multiples of the discretisation time T_{d}: i.e., $k \cdot T_{\mathrm{d}}$ and $(k-1) \cdot T_{\mathrm{d}}$, respectively.

For the discrete-time state-space model of equation (14), the two stages (i.e., *prediction* and *correction*) of the Kalman filter can be performed, see for example Kalman (1960); Grewal and Andrews (2001); Simon (2006). Thus, the Kalman filter estimates the augmented state column matrix

$$\hat{\bar{\mathbf{x}}}_k = \begin{bmatrix}\hat{\phi}_k\\ \hat{\dot{\phi}}_k\\ \hat{T}_{\mathrm{l}k}\end{bmatrix} \tag{15}$$

at every instant of time k, where the estimated state variables consist of the twist angle $\hat{\phi}_k$, the twist angle velocity $\hat{\dot{\phi}}_k$ and also the required load torque $\hat{T}_{\mathrm{l}k}$.

The above described Kalman filter based load torque estimation method using the SDOF filter model from Section 2.1 was implemented in *Matlab* (The MathWorks, Inc. (2021)).

3 Test rig set-up

The basic functioning of the proposed load torque estimation method is verified on basis of powertrain test rig measurements of the ERAD of a Renault Twizy 80. The Renault Twizy 80 is a rear-wheel drive (RWD) BEV of the microcar segment with a top speed of 80 $\frac{\mathrm{km}}{\mathrm{h}}$.

Its propulsion is accomplished by an elastically mounted ERAD, consisting of a $13\,\mathrm{kW}$ and $57\,\mathrm{Nm}$ asynchronous electric motor, a reduction gear, a differential and drive shafts, cf. *Renault Twizy Technical Data* (Renault Group, (2021)). Additionally, in Appendix A, the torque–speed characteristic curve of the asynchronous electric motor is visualised. As described above, the elastic mounting between the ERAD and the chassis is provided by rubber sleeve bushings in a three point mounting concept, see left hand side of Figure 7.

For this work, the Twizy ERAD was installed on a powertrain test rig. Here, the dynos on the wheel-side ends of both drive shafts enabled the adjustment of the load torque as also the rotational speeds of the drive shafts. In contrast to standard powertrain test rig measurements, the ERAD housing was elastically mounted to the test rig environment via the corresponding rubber sleeve bushings, see right hand side of Figure 7. In Kang and Gu (2020), a similar test rig set-up was used to assess the noise vibration harshness (NVH) properties of an electric axle drive.

Figure 7 Basic principle of the elastically mounted Twizy ERAD within the vehicle (left hand side) and the conversion to an elastically mounted ERAD at the powertrain test rig (right hand side) (see online version for colours)

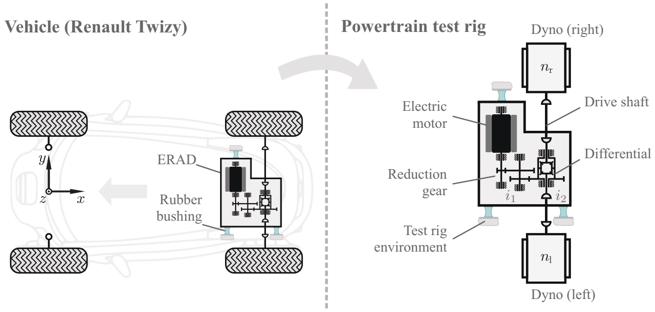

Due to this elastic mounting at the powertrain test rig, there is a relative movement of the ERAD housing with respect to the test rig environment when a torque is transmitted from the electric motor to the dynos. The task of the test rig measurements described below was to determine this six DOF motion with aid of six linear motion position sensors of type *Variohm PZ12A* (Variohm Eurosensor Ltd (2021)). Furthermore, the load torque was also measured with help of two torque transducers of type *HBM T12* (Hottinger Brüel & Kjaer GmbH (2021)). As additional influencing variables, the rotational speeds of both drive shafts were measured. The sensor signals were acquired using the data acquisition system *DEWE-800* (DEWETRON GmbH (2021)) providing signal synchronisation and suitable anti-aliasing filters. All sensor signals were outputted with a rate of $20\,\mathrm{kHz}$. More detailed information about the sensors used, can be found in Appendix B.

Figure 8 shows the set-up of the powertrain test rig with installed Twizy ERAD. The inverter within the power electronics converts the direct current from the battery (not visualised) to a three-phase alternating current, which is used for the operation of the asynchronous electric motor. The two dynos on the wheel-side ends of the drive shafts enable a feedback control of the corresponding rotational speeds. Furthermore, the different sensors (i.e., position, torque and rotational speed) as also the rubber sleeve bushings are shown.

Figure 8 Set-up of the powertrain test rig with installed Twizy ERAD (see online version for colours)

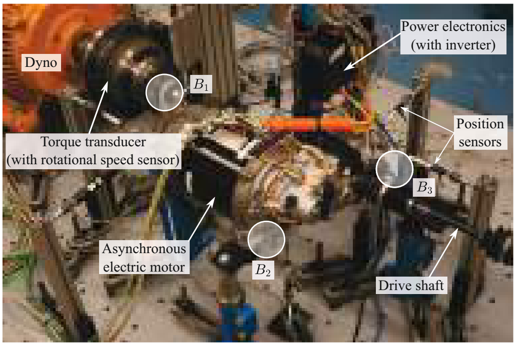

In Figure 9, the installation locations of the six positions sensors are visualised with help of a computer-aided design (CAD) model of the Twizy ERAD. In order to obtain a high signal-to-noise ratio, the positions sensors were installed at three different positions, at which various directions were measured:

- *Position 1*: y and z directions.
- *Position 2*: z direction.
- *Position 3*: x, y and z directions.

Figure 9 Position sensor locations at the Twizy ERAD (see online version for colours)

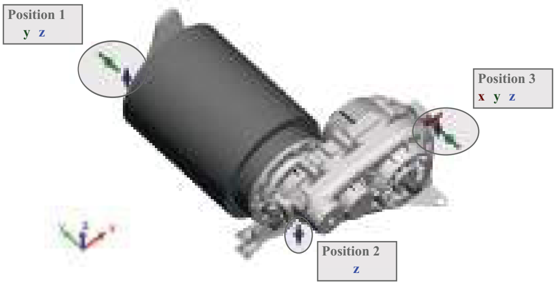

Based on the described test rig set-up, several types of measurements for different aims were performed. Table 1 shows the corresponding test plan, i.e., a list of test manoeuvres to be carried out. First, the accelerator pedal step measurements were used for the determination of the load torque dynamics of the Twizy ERAD. This facilitates the definition of a bandwidth requirement for the proposed load torque estimation method. On the other hand, the accelerator pedal ramp measurements were used for the parameter identification within the simulation–measurement adjustment process. The corresponding verification of the simulation–measurement adjustment was carried out with aid of the *Worldwide harmonized Light vehicles Test Procedure* (WLTP, Class 1) manoeuvre. Finally, the validation of the proposed load torque estimation method was performed with the accelerator pedal sine measurements as also the WLTP measurements.

Table 1 Test plan for the powertrain test rig measurements

Type	*No.*	*Description*	*Aims*
Step	1	Several accelerator pedal steps at dyno rotational speeds of 280 min^{-1}	• *Determination of the load torque dynamics*
	2	Several accelerator pedal steps at dyno rotational speeds of 560 min^{-1}	
Ramp	3	Accelerator pedal ramp from 0 % to 100 % in 60 s at dyno rotational speeds of 280 min^{-1}	• *Parameter identification (sim.–meas. adjustment)*
	4	Accelerator pedal ramp from 0 % to 100 % in 60 s at dyno rotational speeds of 560 min^{-1}	
	5	Accelerator pedal ramp from 0 % to 100 % in 20 s at dyno rotational speeds of 280 min^{-1}	
	6	Accelerator pedal ramp from 0 % to 100 % in 20 s at dyno rotational speeds of 560 min^{-1}	
Sine	7	Accelerator pedal sine from 5 % to 25 % with 0.1 Hz at dyno rotational speeds of 280 min^{-1}	• *Validation of the load torque estimation method*
	8	Accelerator pedal sine from 5 % to 25 % with 0.1 Hz at dyno rotational speeds of 560 min^{-1}	
WLTP	9	Worldwide harmonized light vehicle test procedure (WLTP, Class 1)	• *Verification of the sim.–meas. adjustment* • *Validation of the load torque estimation method*

Figure 10 shows the input signals (i.e. accelerator pedal value α_p and dyno rotational speed n_d). Here, no rotational speed differences between the left and right dyno were applied, thus it holds: $n_\mathrm{l} = n_\mathrm{d}$ and $n_\mathrm{r} = n_\mathrm{d}$.

Figure 10 Excerpt of test input signals: (a) accelerator pedal step; (b) accelerator pedal ramp; (c) accelerator pedal sine and (d) WLTP (see online version for colours)

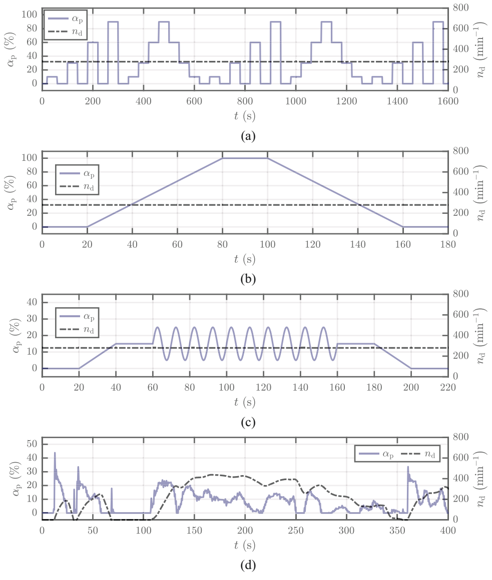

(a)

(b)

(c)

(d)

4 Measurement output

In this section some decisive measurement results and their processing are presented. First, in Section 4.1, the results of the accelerator pedal step measurements were used for the determination of the load torque dynamics of the Twizy ERAD. Furthermore, the simulation–measurement adjustment was performed, see Section 4.2. The outcome of this was a measurement-adjusted simulation model, which subsequently was used for the validation of the proposed load torque estimation method.

4.1 Determination of the load torque dynamics

The determination of the load torque dynamics of the Twizy ERAD was carried out by evaluating the accelerator pedal step measurements. Here, the measured load torques of tip-in and tip-out tests were modelled with a PT1 element. In addition to the PT1 element, a constant time delay of $35\ \mathrm{ms}$ was used in order to model the lag between a accelerator pedal step and the begin of the corresponding load torque response. The parameters of the PT1 element (i.e., gain K and time constant τ) were found using a Matlab optimisation routine. Figure 11 shows the results for tip-in and tip-out tests at different rotational speeds. It can be seen that the measured load torque can be well represented by the PT1 element with appropriate parameters.

Figure 11 Determination of the load torque dynamics with help of accelerator pedal step measurements: (a) *tip-in* at *low* rotational speed ($n_\mathrm{d} = 280\ \mathrm{min}^{-1}$); (b) *tip-in* at *high* rotational speed ($n_\mathrm{d} = 560\ \mathrm{min}^{-1}$); (c) *tip-out* at *low* rotational speed ($n_\mathrm{d} = 280\ \mathrm{min}^{-1}$) and (d) *tip-out* at *high* rotational speed ($n_\mathrm{d} = 560\ \mathrm{min}^{-1}$) (see online version for colours)

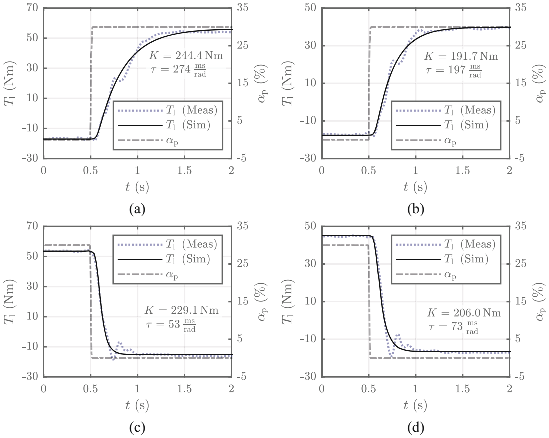

The identified parameters were confirmed through reproductive measurements, see Table 2. There, maximum load torque dynamics for tip-in and tip-out tests can be found via the evaluation of the corresponding cut-off frequencies:

- *Tip-in*: $\tau^\mathrm{In}_\mathrm{Min} = 195\ \frac{\mathrm{ms}}{\mathrm{rad}} \quad \Rightarrow \quad f^\mathrm{In}_\mathrm{Max} = \frac{1}{2 \cdot \pi \cdot \tau^\mathrm{In}_\mathrm{Min}} \approx 0.8$ Hz.
- *Tip-out*: $\tau^\mathrm{Out}_\mathrm{Min} = 53\ \frac{\mathrm{ms}}{\mathrm{rad}} \quad \Rightarrow \quad f^\mathrm{Out}_\mathrm{Max} = \frac{1}{2 \cdot \pi \cdot \tau^\mathrm{Out}_\mathrm{Min}} \approx 3.0$ Hz.

Thus, it can be seen that the effective load torque dynamics is limited in any case to ca. 3 Hz, which can be used as approximate bandwidth limit for the proposed load torque estimation method. This order of magnitude can be justified since passenger cars typically limit the effective torque dynamics to such low-frequency ranges in order to avoid unwanted load alternating vibrations, cf. Zeller (2018); Koch et al. (2020).

Table 2 Identified PT1 parameters of the modelled load torque dynamics with respect to accelerator pedal steps

Manoeuvre	*No.*	K (Nm)	τ $\left(\frac{\mathrm{ms}}{\mathrm{rad}}\right)$
Tip-in at *low* rotational speed ($n_\mathrm{d} = 280\ \mathrm{min}^{-1}$)	1	244.4	274
	2	244.5	271
	3	242.7	266
	Mean	*243.9*	*270*
Tip-in at *high* rotational speed ($n_\mathrm{d} = 560\ \mathrm{min}^{-1}$)	1	191.7	197
	2	190.7	195
	3	191.4	194
	Mean	*191.3*	*195*
Tip-out at *low* rotational speed ($n_\mathrm{d} = 280\ \mathrm{min}^{-1}$)	1	229.1	52
	2	229.8	51
	3	231.4	55
	Mean	*230.1*	*53*
Tip-out at *high* rotational speed ($n_\mathrm{d} = 560\ \mathrm{min}^{-1}$)	1	206.0	73
	2	202.3	76
	3	203.9	76
	Mean	*204.1*	*75*

4.2 Simulation–measurement adjustment

In order to obtain more flexibility, a hybrid experimental–numerical approach was used for the validation of the load torque estimation method. Here, the basic idea is to develop a MBS simulation model which behaves approximately the same like the measured Twizy ERAD at the powertrain test rig. Then the benefits of simulation, such as fast parameter variation or simple configuration changes can be applied. In this section, the simulation–measurement adjustment process is described, which results in a measurement-adjusted MBS simulation model with fitted parameters.

Figure 12 shows the structure of the MBS model used, which was developed with the commercial, general purpose MBS software *Simpack* (Dassault Systèmes Simulia Corp., 2021); Rulka (1990) and Kortüm et al. (1996)). The three rubber sleeve bushings are modelled via Kelvin–Voigt elements. The torque transfer from the asynchronous electric motor via the reduction gear and the differential to the drive shafts are represented through appropriate gear modelling elements of the Simpack library. The – not visualised – dynos enable the right rotational speeds of both drive shafts with aid of proportional–integral (PI) controllers.

Figure 12 MBS simulation model of the Twizy ERAD at the powertrain test rig (see online version for colours)

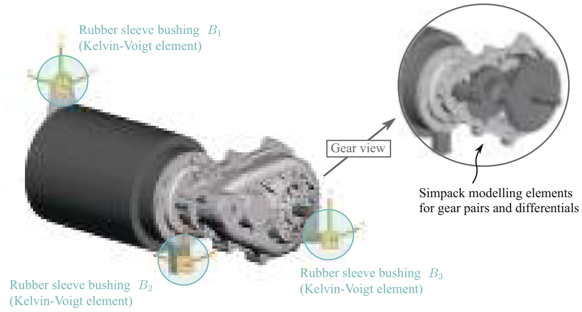

In Figure 13, the principle of the simulation–measurement adjustment is shown. The base MBS model with its initial parameterisation is formulated in state-space representation, which enables a fast simulation within Matlab/Simulink. Using the same inputs for simulation and measurement, an objective function is defined based on the differences of simulated and measured outputs of the six position sensors in a least squares sense. This objective function is minimised iteratively with help of a Matlab optimisation algorithm, where the translational stiffnesses of all three rubber sleeve bushings are used as the nine decision variables. The optimisation routine uses the accelerator pedal ramp measurements yielding a set of fitted bushing stiffnesses. With this, the MBS model is parametrised resulting in a measurement-adjusted MBS model, which exhibits nearly the same movement like the real Twizy ERAD.

Figure 13 Principle of the simulation–measurement adjustment process (see online version for colours)

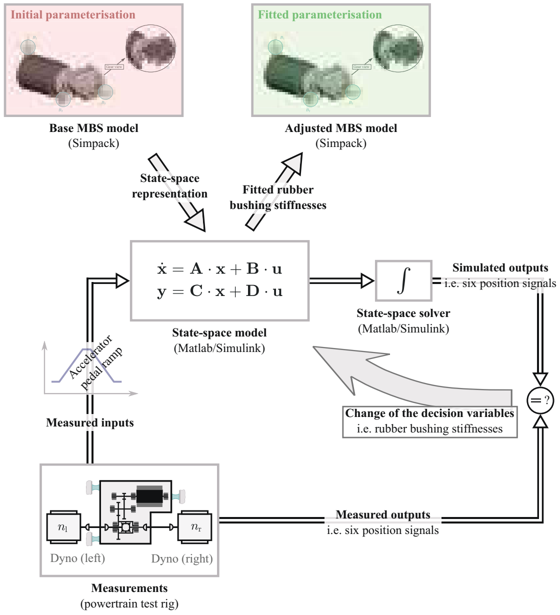

In Figure 14, the objective function contributions (i.e., the six position sensor signals) are shown for the final optimisation step. It can be clearly seen that the differences between simulated and measured position sensor signals are only marginal, which proves the basic functioning of the optimisation-based simulation–measurement adjustment process. The numbers (i.e., 3, 4, 5 and 6) in Figure 14 refer to the test numbers in Table 1.

Figure 14 Objective function contributions for the final optimisation step (see online version for colours)

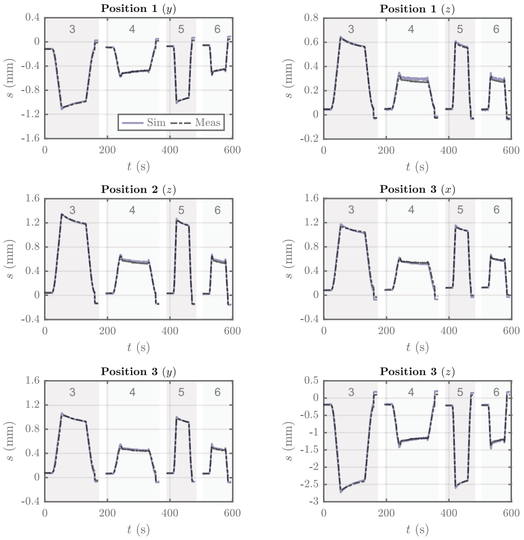

The results of the simulation–measurement adjustment process are listed in Table 3.

Table 3 Results of the simulation–measurement adjustment process

Bushing	*Stiffness symbol*	*Value*	*Unit*
B_1	$k_{1\,x}$	438	$\frac{\mathrm{N}}{\mathrm{mm}}$
	$k_{1\,y}$	94	$\frac{\mathrm{N}}{\mathrm{mm}}$
	$k_{1\,z}$	722	$\frac{\mathrm{N}}{\mathrm{mm}}$
B_2	$k_{2\,x}$	1186	$\frac{\mathrm{N}}{\mathrm{mm}}$
	$k_{2\,y}$	227	$\frac{\mathrm{N}}{\mathrm{mm}}$
	$k_{2\,z}$	525	$\frac{\mathrm{N}}{\mathrm{mm}}$
B_3	$k_{3\,x}$	1929	$\frac{\mathrm{N}}{\mathrm{mm}}$
	$k_{3\,y}$	1273	$\frac{\mathrm{N}}{\mathrm{mm}}$
	$k_{3\,z}$	293	$\frac{\mathrm{N}}{\mathrm{mm}}$

As it is good practice, the simulation–measurement adjustment was also verified with another manoeuvre, namely, the WLTP test. Here, the mean simulation–measurement deviation per time step k was carried out for all six position sensor signals s_j, with $j = \{1\,y, 1\,z, 2\,z, 3\,x, 3\,y, 3\,z\}$:

$$\bar{e}_j = \frac{1}{N} \cdot \sum_{k=1}^{N} \left| s_{j\,k}^{\mathrm{Sim}} - s_{j\,k}^{\mathrm{Meas}} \right|, \tag{16}$$

where N denotes the number of time steps. As it can be seen in Figure 15, the mean deviations are limited to an absolute value of 0.03 mm and a relative value of $2.2\,\%$ with respect to the total signal range. Due to these favourable results, the measurement-adjusted MBS simulation model can be used for the method validation in the next section with good conscience. A list of the main simulation parameters of the measurement-adjusted MBS model can be found in Appendix C.

Figure 15 Verification of the simulation–measurement adjustment process with aid of the WLTP test (see online version for colours)

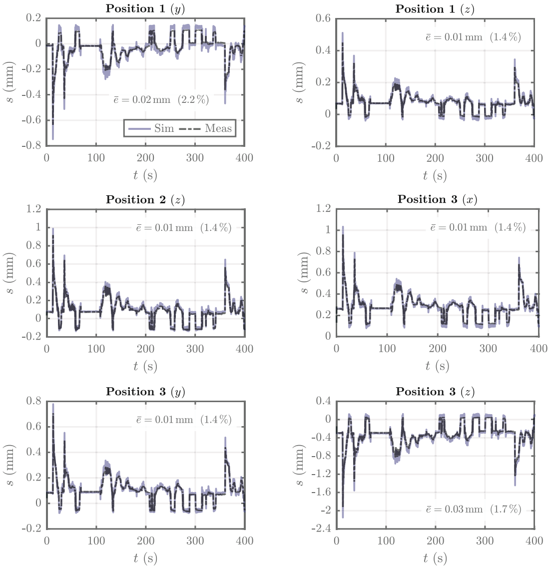

5 Method validation

The Kalman filter based load torque estimation method presented in Section 2 was verified with help of a hybrid experimental–numerical validation procedure. Hence, the measurement-adjusted MBS simulation model from Section 4.2 was used as reference model. This can be justified due to the proved similar six DOF movement of the reference model and the real Twizy ERAD at the powertrain test rig. Furthermore, based on the mismatch between sophisticated reference model and, on the other hand, simple SDOF filter model, a robust method validation can be ensured. The simulated load torque of the reference model is thus regarded as true value. Moreover, the ERAD twist motion of the reference model was used as Kalman filter input. In detail, a zero-mean white Gaussian noise was added to the simulated twist angle about the TRA in order to ensure a realistic sensor behaviour. The standard deviation of this measurement noise was set to $\sigma_\phi = 0.029\,\mathrm{deg}$, which represents approximately $3\,\%$ of the total sensor measurement range. Based on that, the twist angle velocity was calculated recursively via backward differentiation. This emulates a possible measurement application in series production vehicles with only one contactless angle sensor aligned with respect to the TRA. Here, standard automotive angle sensors can be applied, which are well-known from measurement tasks for the angular position determination of pedals or steering wheels.

For this, an angle sensor about the numerically calculated TRA was implemented within the reference model (i.e., TRA-based angle sensor). Additionally, another angle sensor was modelled on an arbitrary location on the ERAD housing for comparison purposes, see Figure 16. As real contactless automotive angle sensors, both consist of two parts: One is attached on the ERAD housing and the second is fixed at the test rig environment.

Figure 16 MBS models with numerically determined TRA and the two implemented angle sensors (see online version for colours)

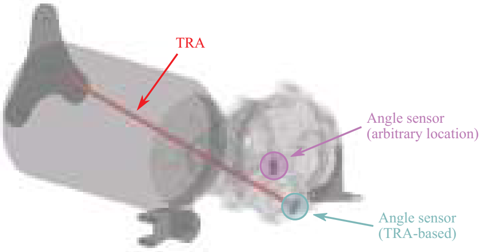

Using these two angle sensors within the reference model, the determined TRA and the corresponding ERAD motion can be verified. For this, all three Cardan angles of both implemented angle sensors were evaluated. As it can be clearly seen in Figure 17, the TRA-based angle sensor shows almost solely a signal for α, that is the twist about the TRA. Whereas, the arbitrary placed angle sensor has non-trivial signals for all three Cardan angles. Thus, the claim from the beginning of this paper holds: The six DOF movement of the elastically mounted ERAD under torque load can be approximately reduced to a twist motion about the TRA. Consequently, the proposed simple SDOF filter model from Section 2.1 should be sufficient.

Furthermore, in Figure 18, the influences of stochastic road irregularities on the twist angle signal were evaluated. For this purpose, the test rig-based points of application of the three elastomer mounts were excited with aid of rheonomic constraints in the z directions. The corresponding z motions were calculated in advance with help of a full vehicle MBS model with 87 DOFs. Here, the crossing of the following road classes with a vehicle velocity of $40\,\frac{\mathrm{km}}{\mathrm{h}}$ were simulated:

- ‘road a’: no road irregularities,
- ‘road b’: cement concrete and
- ‘road c’: macadam.

In Figure 18, the α Cardan angles of the TRA-based angle sensor were visualised, where the deviations based on the stochastic road irregularities were limited to approximately

0.03 deg. Since this is in the same order of magnitude as a realistic sensor noise, no prohibitive impacts are to be expected based on stochastic road excitations. This is the same conclusion as in Kalcher et al. (2022), where a more detailed analysis of the influences of stochastic as also deterministic road excitations on the proposed load torque estimation method can be found.

Figure 17 Cardan angle signals: (a) angle sensor with arbitrary location and (b) angle sensor with TRA-based location (see online version for colours)

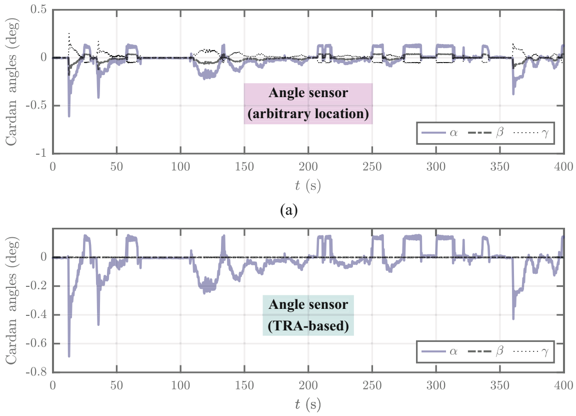

(a)

(b)

Figure 18 Influence analysis for stochastic road excitations: (a) load torque time history and (b) α Cardan angles for three road classes (see online version for colours)

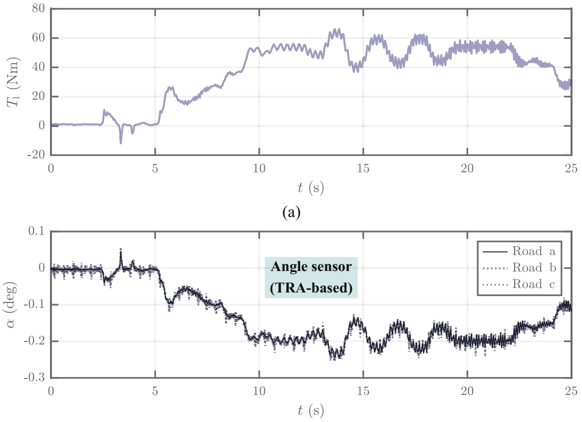

(a)

(b)

After the verification of the ERAD movement, the proposed Kalman filter based load torque estimation method was validated. Here, the following load torque time histories are analysed:

- '*True*': signal of the reference model.
- '*KF*': estimation of the proposed Kalman filter based method.
- '*Char. curve*': estimation of a simple characteristic curve approach.

Where the simple characteristic curve approach uses the torsional spring stiffness from Section 2.1, to relate the measured noisy twist angle about the TRA to an associated load torque estimation. Further on, the similarities as also the deviations of the true signal and the two estimations are analysed. For this, it is necessary to define the load torque differences as follows:

$$\Delta T_{\mathrm{l}\,k} := T_{\mathrm{l}\,k} - \hat{T}_{\mathrm{l}\,k}, \tag{17}$$

where $T_{\mathrm{l}\,k}$ and $\hat{T}_{\mathrm{l}\,k}$ are the true load torque and the estimated load torque at time instant k, respectively. According to the specific evaluation, for the estimated load torque, the signal of the proposed Kalman filter based method or the signal of the characteristic curve approach was used. Furthermore, with the normalised mean square error (NMSE) another evaluation variable is introduced, cf. Kalcher et al. (2022):

$$\begin{aligned} \mathrm{NMSE} &= \frac{1}{N_{\Delta t}} \cdot \sum_{k}^{(\Delta t)} \frac{\left(\Delta T_{\mathrm{l}\,k}\right)^2}{T_{\mathrm{l\,Max}} - T_{\mathrm{l\,Min}}}, \\ T_{\mathrm{l\,Max}} &:= \max_{1 \le k \le N} \left(T_{\mathrm{l}\,k}\right), \\ T_{\mathrm{l\,Min}} &:= \min_{1 \le k \le N} \left(T_{\mathrm{l}\,k}\right), \end{aligned} \tag{18}$$

where $N_{\Delta t}$ is number of time steps within the moving mean period Δt. If not otherwise stated, for the further evaluations, Δt is set to 3 s. Furthermore, by default, the Kalman filter was run in Matlab with a discretisation time of $T_{\mathrm{d}} = 10$ ms.

First, the basic functioning of the proposed Kalman filter based load torque estimation method is tested with a low-frequency (i.e. 0.1 Hz) harmonic torque signal. In Figure 19, it can be seen that both estimation methods can follow the basic form of the true signal. However, based on the underlying Kalman filter, the signal of the proposed load torque estimation method has a significantly lower noise. This is also evident for the NMSE time histories as well as the load torque differences. Additionally, the probability density functions (PDFs) $f\left(\Delta T_{\mathrm{l}}\right)$ of the load torque differences are displayed. Again, the considerably reduced noise for the proposed load torque estimation method is apparent. This can also be seen in the associated standard deviations σ: with the values 2.6 Nm for the proposed load torque estimation method and 6.6 Nm for the characteristic curve approach.

After evaluating the low-frequent basic functioning, the proposed load torque estimation method is validated with a transient signal, namely the WLTP manoeuvre. Here, the same statement holds: In general, both estimation methods can represent the basic true signal form, but only the proposed load torque estimation method provides a suitable estimate with only low noise, see Figure 20. For the WLTP manoeuvre, the standard deviations of the torque differences yield 2.5 Nm and 6.5 Nm for the proposed load torque estimation method and the characteristic curve approach, respectively.

Figure 19 Load torque estimations for a low-frequency (i.e., 0.1 Hz) sine signal: (a) load torque time histories; (b) time histories of the NMSEs as well as (c) time histories and PDFs of the load torque differences

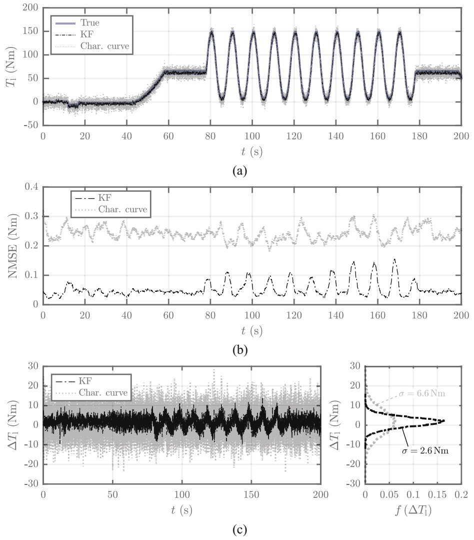

Figure 20 Load torque estimations for the WLTP manoeuvre: (a) load torque time histories; (b) time histories of the NMSEs as well as (c) time histories and PDFs of the load torque differences

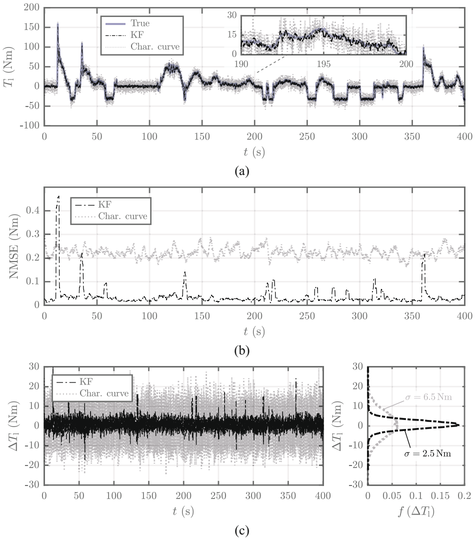

As further investigation, the asynchronous electric motor of the reference model was operated with a swept-frequency sine torque signal with a constant amplitude of $10\ \mathrm{Nm}$. Due to the limited torque dynamics of the real asynchronous electric motor, this evaluation could only be carried out owing to the experimental–numerical validation deployed. Here, the relative kinematics of the TRA-based angle sensor is analysed. More precisely, the coordinate differences of the two sensor parts to each other were evaluated. This is important, because real two-part angle sensors lose accuracy or fail completely, if the translational differences between the two parts become too large. The sensor manufacturer *ASM*, for instance, defines such functional limits for the translational differences, cf. (ASM Automation Sensorik (2021)):

- *Longitudinal direction*: $x \leq 10.5$ mm.
- *Transverse direction*: $y \leq 0.5$ mm and $z \leq 0.5$ mm.

Figure 21 shows that these limits are met over a wide frequency range. Even in the vicinity of the first eigenmode peak at 20.4 Hz, these requirements are fulfilled. Whereby additionally, all eigenmodes of the Twizy ERAD are over 20 Hz (see Appendix D), which is significantly above the determined load torque dynamics of the Twizy ERAD with approximately 3 Hz. But this argument holds also in general, as typical ERADs have eigenmodes over 5 Hz, cf. Roth et al. (2019).

Figure 21 Relative kinematics of the TRA-based angle sensor with respect to a motor torque sweep signal (see online version for colours)

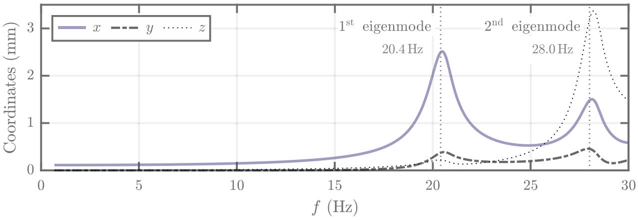

Finally, some influence analyses for the load torque estimations are presented. Here, the estimation results of several WLTP manoeuvres were evaluated with respect to the NMSE over the total time span (i.e., $N_{\Delta t} = N$). Thus, the estimation quality can be characterised by only one scalar value. At first, the standard discretisation time of 10 ms was varied between 1 ms and 1 s. In the left hand side of Figure 22, it can be seen that the following plausible relationship holds for the proposed Kalman filter based load torque estimation method: The smaller the discretisation time, the smaller the NMSE. Whereas the variation of the discretisation time does not affect characteristic curve approach results. Moreover, for practical discretisation times under 100 ms, the proposed load torque estimation method performs significantly better than the characteristic curve approach. On the other hand, the influence of the measurement noise was evaluated. In the right hand side of Figure 22, it can be seen that the Kalman filter handles the sensor noise considerably better than the characteristic curve approach. Only with an unrealistically small measurement noise, the results are comparable. Furthermore, the consequences of more general Kalman filter versions were analysed. As the filter model considered is completely linear (cf. equation (9)), the application of an EKF does not make sense because the model can not be further linearised. However, since its completely different approach via unscented transformations, it is worth to analyse the UKF torque estimation. In Figure 22, the results of an UKF implementation were compared with the Kalman filter results. It can be seen that the NMSEs are almost the same for both versions, but with a significantly lower computational load for the simple Kalman filter.

Figure 22 Load torque estimation influence analyses regarding the WLTP manoeuvre: (a) NMSE vs. discretisation time T_d and (b) NMSE vs. standard deviation of the angle sensor noise σ_ϕ (see online version for colours)

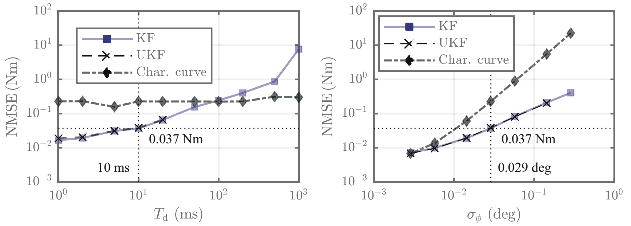

(a) (b)

6 Conclusions

In this work, a Kalman filter based virtual sensing technique for the load torque estimation of electric axle drives was developed and verified with help of a hybrid experimental–numerical validation. For this, the ERAD of a Renault Twizy 80 was installed with its three rubber sleeve bushings at a powertrain test rig. By performing several test manoeuvres (e.g., accelerator pedal steps, WLTP, etc.), the load torque and the six DOF motion of the ERAD housing as also additional influencing variables (i.e., drive shafts' rotational speeds) were measured by appropriate sensors. These test rig measurement results were used in conjunction with a Simpack MBS simulation model within an optimisation-based simulation–measurement adjustment process. This resulted in a measurement-adjusted reference model, which was used for the validation of the proposed load torque estimation method.

First, is was checked on basis of the reference model that the simple SDOF filter model is sufficient to describe the movement of the ERAD housing adequately. Subsequently, the basic functioning of the proposed load torque estimation method was proved by evaluating test manoeuvres for quasi-static as also transient excitations. The investigations revealed favourable results even in the case of reasonable effective torque dynamics (up to 3 Hz) and realistic sensor noise. Furthermore, influence analyses regarding the discretisation time of the Kalman filter and the amount of sensor noise were performed. This consolidates the method validation and also allows requirement definitions for a practical implementation.

In conclusion, the principle of the proposed load torque estimation method was proved on basis of powertrain test rig measurements. Based on these, no prohibitive impacts arose. As a next step, future works should focus on the application and the corresponding verification of this method within electric vehicles.

Acknowledgements

This work was supported by the Austrian Research Promotion Agency (FFG) within the programs *Forschungspartnerschaften* and *Innovationsscheck*.

References

Alkhatib, F. (2013) *Techniques for Engine Mount Modeling and Optimization*, PhD Thesis, University of Wisconsin, Milwaukee, WI, USA.

Bachinger, M., Stolz, M. and Horn, M. (2014) 'Fixed step clutch modeling and simulation for automotive real-time applications', *2014 American Control Conference*, 4–6 June, Portland, OR, USA, pp.2593–2599.

Chauvin, J., Corde, G., Moulin, P., Castagné, M., Petit, N. and Rouchon, P. (2004) 'Real-time combustion torque estimation on a Diesel engine test bench using time-varying Kalman filtering', *Proceedings of the 43rd IEEE Conference on Decision and Control*, Vol. 2, pp.1688–1694.

Courteille, E., Mortier, F., Leotoing, L., and Ragneau, E. (2005) *Multi-Objective Robust Design Optimization of an Engine Mounting System*, SAE Technical Paper, No. 2005-01-2412.

Cumbo, R., Tamarozzi, T., Janssens, K. and Desmet, W. (2019) 'Kalman-based load identification and full-field estimation analysis on industrial test case', *Mechanical Systems and Signal Processing*, Vol. 117, pp.771–785.

Doerr, J., Attensperger, T., Wittmann, L. and Enzinger, T. (2018) 'The new electric axle drives from Audi', *MTZ worldwide*, Vol. 79, No. 6, pp.18–25.

Doerr, J., Fröhlich, G., Stroh, A. and Baur, M. (2020) 'Das elektrische Antriebssystem mit Drei-Motor-Layout im Audi E-tron S', *MTZ-Motortechnische Zeitschrift*, Vol. 81, No. 7, pp.18–27.

Domian, H.J., Ketteler, K.H. and Scharr, S. (2013) 'Electric axle drive module for high speeds', *ATZ worldwide*, Vol. 115, No. 12, pp.10–13.

Eghtessad, M., Meier, T., Rinderknecht, S. and Küçükay, F. (2015) 'Antriebsstrangoptimierung von Elektrofahrzeugen', *ATZ-Automobiltechnische Zeitschrift*, Vol. 117, No. 9, pp.78–85.

Forrier, B., Naets, F. and Desmet, W. (2017) 'Broadband load torque estimation in mechatronic powertrains using nonlinear Kalman filtering', *IEEE Transactions on Industrial Electronics*, Vol. 65, No. 3, pp.2378–2387.

Forrier, B. (2018) *Virtual Torque Sensing: A Model-Based Approach for Indirect Measurement of Dynamic Operational Loads on Mechatronic Powertrains*, PhD Thesis, KU Leuven, Leuven, Belgium.

Gavric, L. (2020) 'NVH refinement issues for BEV', in Siebenpfeiffer, W. (Ed.), *Automotive Acoustics Conference 2019*, Springer, Wiesbaden, Germany, pp.1–9.

Grewal, M.S. and Andrews, A.P. (2001) *Kalman Filtering: Theory and Practice Using Matlab*, 2nd ed., John Wiley & Sons, New York, NY, USA.

Hauptmann, R. (2018) *System Architecture and Potential Analysis of Electric Axle Drives*, Master's Thesis, Graz University of Technology, Graz, Austria.

Helm, S., Kozek, M. and Jakubek, S. (2012) 'Combustion torque estimation and misfire detection for calibration of combustion engines by parametric Kalman filtering', *IEEE Transactions on Industrial Electronics*, Vol. 59, No. 11, pp.4326–4337.

Höfer, A., Peschkow, W. and Hamon, P. (2020) 'Elektrische Achsen im Spannungsfeld von NVH, Wirkungsgrad und Leistungsdichte', *ATZ-Automobiltechnische Zeitschrift*, Vol. 122, No. 4, pp.48–53.

Hofmann, P. (2014) *Hybridfahrzeuge: Ein alternatives Antriebssystem für die Zukunft*, 2nd ed., Springer, Vienna, Austria.

Jakubek, S. and Fleck, A. (2009) 'Schäzung des inneren Drehmoments von Verbrennungsmotoren durch parameterbasierte Kalmanfilterung: Inner Torque Estimation for Combustion Engines by Parametric Kalman Filtering', *at-Automatisierungstechnik*, Vol. 57, No. 8, pp.395–402.

Jeong, T. and Singh, R. (2000) 'Analytical methods of decoupling the automotive engine torque roll axis', *Journal of Sound and Vibration*, Vol. 234, No. 1, pp.85–114.

Julier, S.J., Uhlmann, J.K. and Durrant-Whyte, H.F. (1995) 'A new approach for filtering nonlinear systems', *Proceedings of the 1995 American Control Conference*, Vol. 3, pp.1628–1632.

Julier, S.J. and Uhlmann, J.K. (2004) 'Unscented filtering and nonlinear estimation', *Proceedings of the IEEE*, Vol. 92, No. 3, pp.401–422.

Kalcher, R., Ellermann, K. and Kelz, G. (2022) 'Load torque estimation for an automotive electric rear axle drive by means of virtual sensing using Kalman filtering', *International Journal of Vehicle Performance*, Vol. 8, No. 1, pp.1–30.

Kalman, R.E. (1960) 'A new approach to linear filtering and prediction problems', *Trans. ASME J. Basic Eng.*, Vol. 82, pp.34–45.

Kang, Q. and Gu, P. (2020) 'NVH design criterion of electric powertrain mounts', in Siebenpfeiffer, W. (Ed.): *Automotive Acoustics Conference 2019*, Springer, Wiesbaden, Germany, pp.10–27.

Kasper, R. and Schünemann, M. (2012) '5. Elektrische Fahrantriebe: Topologien und Wirkungsgrad', *MTZ-Motortechnische Zeitschrift*, Vol. 73, No. 10, pp.802–807.

Khiar, D., Lauber, J., Floquet, T. and Guerra, T.M. (2005) 'An observer design for the instantaneous torque estimation of an IC engine', *2005 IEEE Vehicle Power and Propulsion Conference*, September 7–9, Chicago, IL, USA, pp.391–395.

Kiencke, U. (1999) 'Engine misfire detection', *Control engineering practice*, Vol. 7, No. 2, pp.203–208.

Koch, A., Schulz, L., Jakstas, G. and Falkenstein, J. (2020) 'Drivability optimization by reducing oscillation of electric vehicle drivetrains', *World Electric Vehicle Journal*, Vol. 11, No. 4, pp.68–86.

Kortüm, W., Sachau, D. and Schwertassek, R. (1996) 'Analysis and design of flexible and controlled multibody systems with SIMPACK', *Space Technology*, Vol. 5, No. 16, pp.355–364.

Lennström, D. (2015) *Assessment and Control of Tonal Components in Electric Vehicles*, PhD Thesis, Lulea University of Technology, Lulea, Sweden.

Lex, C. (2015) *Maximum Tire-Road Friction Coefficient*, PhD Thesis, Graz University of Technology, Graz, Austria.

Lieske, D., Landes, D. and Fischer, J. (2020) 'Optimization of the powertrain noise for the electric vehicle Mercedes-Benz EQC', *ATZ Worldwide*, Vol. 122, No. 3, pp.56–61.

Lourens, E., Reynders, E., De Roeck, G., Degrande, G. and Lombaert, G. (2012) 'An augmented Kalman filter for force identification in structural dynamics', *Mechanical Systems and Signal Processing*, Vol. 27, pp.446–460.

Maes, K., Karlsson, F. and Lombaert, G. (2019) 'Tracking of inputs, states and parameters of linear structural dynamic systems', *Mechanical Systems and Signal Processing*, Vol. 130, pp.755–775.

Mühlberg, G., Hackmann, W. and Buzziol, K. (2017) 'Hoch integrierter elektrischer Antriebsstrang', *ATZelektronik*, Vol. 12, No. 4, pp.42–45.

Naets, F., Pastorino, R., Cuadrado, J. and Desmet, W. (2014) 'Online state and input force estimation for multibody models employing extended Kalman filtering', *Multibody System Dynamics*, Vol. 32, No. 3, pp.317–336.

Naets, F., Cuadrado, J. and Desmet, W. (2015a) 'Stable force identification in structural dynamics using Kalman filtering and dummy-measurements', *Mechanical Systems and Signal Processing*, Vol. 50, pp.235–248.

Park, J.Y. and Singh, R. (2007) *Effect of Engine Mount Damping on the Torque Roll Axis Decoupling*, SAE Technical Paper, No. 2007-01-2418.

Prokhorov, D. (2005) 'Virtual sensors and their automotive applications', *2005 International Conference on Intelligent Sensors, Sensor Networks and Information Processing*, 5–8 December, Melbourne, VIC, Australia, pp.411–416.

Ray, L.R. (1995) 'Nonlinear state and tire force estimation for advanced vehicle control', *IEEE Transactions on Control Systems Technology*, Vol. 3, No. 1, pp.117–124.

Ray, L.R. (1997) 'Nonlinear tire force estimation and road friction identification: simulation and experiments', *Automatica*, Vol. 33, No. 10, pp.1819–1833.

Reif, K. and Dietsche K.H. (2011) *Kraftfahrtechnisches Taschenbuch*, 27th ed., Robert Bosch GmbH (Ed.), Springer, Wiesbaden, Germany.

Risaliti, E., Cornelis, B., Tamarozzi, T. and Desmet, W. (2016) 'A state-input estimation approach for force identification on an automotive suspension component', *Proceedings of the 34th IMAC, A Conference and Exposition on Structural Dynamics 2016*, 25–28 January, Orlando, FL, pp.359–369.

Risaliti, E., Tamarozzi, T., Vermaut, M., Cornelis, B. and Desmet, W. (2019) 'Multibody model based estimation of multiple loads and strain field on a vehicle suspension system', *Mechanical Systems and Signal Processing*, Vol. 123, pp.1–25.

Roth, D., Ehrt, T., Bultel, C. and Kardoes, H. (2019) 'Powertrain mounting systems for electric vehicles', in Siebenpfeiffer, W. (Ed.), *Automotive Acoustics Conference 2017*, Springer, Wiesbaden, Germany, pp.91–106.

Rulka, W. (1990) 'SIMPACK – A computer program for simulation of large-motion multibody systems', In *Multibody Systems Handbook*, Springer, Berlin, Heidelberg, pp. 265–284..

Schaper, U., Sawodny, O., Mahl, T. and Blessing, U. (2009) 'Modeling and torque estimation of an automotive dual mass flywheel', *2009 American Control Conference*, June 10–12, St. Louis, MO, USA, pp.1207–1212.

Schnellbach, A., Hirz, M. and Fabian, J. (2016) 'Comparison of fail-operational software architectures from the viewpoint of an automotive application', *Elektrotechnik und Informationstechnik*, Vol. 133, No. 6, pp.283–293.

Schwartz, J. (2014) *Electric Motor Installation for Improved Vehicle Noise Characteristics*, Master's Thesis, Lund University (LTH), Lund, Sweden.

Siebenpfeiffer, W. (Ed.) (2015) *Fahrerassistenzsysteme und Effiziente Antriebe*, Springer, Wiesbaden, Germany.

Simon, D. (2006) *Optimal state estimation: Kalman, H_∞, and nonlinear approaches*, John Wiley & Sons, Hoboken, NJ, USA.

Smetana, T., Berger, M., Gramann, M. and Mitariu-Faller, M. (2013) 'Modular system for electrical drive axles', *ATZ worldwide*, Vol. 115, No. 9, pp.32–37.

Tschöke, H. and Gutzmer, P. and Pfund, T. (Eds.) (2019) *Elektrifizierung des Antriebsstrangs: Grundlagen - vom Mikro-Hybrid zum vollelektrischen Antrieb*, 3rd ed., Springer, Wiesbaden, Germany.

Wallentowitz, H. and Freialdenhoven, A. (2011) *Strategien zur Elektrifizierung des Antriebsstranges: Technologien, Märkte und Implikationen*, 2nd ed., Springer, Wiesbaden, Germany.

Zeller, P. (Ed.) (2018) *Handbuch Fahrzeugakustik*, 3rd ed., Springer, Wiesbaden, Germany.

Websites

ASM Automation Sensorik (2021) *ASM*, https://www.asm-sensor.com (Accessed 18 April, 2021).

Dassault Systèmes Simulia Corp. (2021) *Simpack*, https://www.simpack.com (Accessed 18 April, 2021).

DEWETRON GmbH (2021) *DEWE-800*, https://www.dewetron.com (Accessed 18 April, 2021).

Renault Group (2021) *Renault Twizy Technical Data*, https://group.renault.com (Accessed 18 April, 2021).

Hottinger Brüel & Kjaer GmbH (2021) *HBM T12 Digital Torque Transducer*, https://www.hbm.com (Accessed 18 April, 2021).

The MathWorks, Inc. (2021) *Matlab*, https://www.mathworks.com (Accessed 18 April, 2021).

Variohm Eurosensor Ltd (2021) *Data sheet for PZ12A*, https://www.variohm.com (Accessed 18 April, 2021).

Appendix

A Electric motor torque–speed characteristics

In Figure A1, the torque–speed characteristic curve of the asynchronous electric motor of the Renault Twizy 80 is shown. It was determined with aid of the manufacturer information about the constant torque region and the maximum rotational speed.

Figure A1 Torque–speed characteristics of the asynchronous electric motor of the Renault Twizy 80 (see online version for colours)

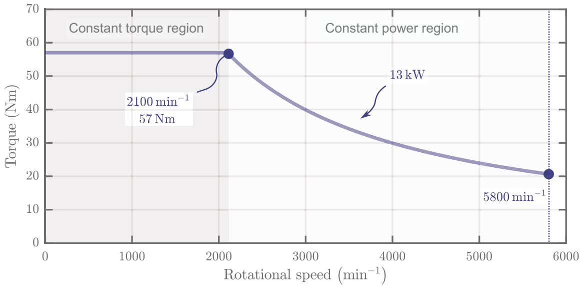

B Sensor data

B1 Linear motion position sensors

For the measurement of the Twizy ERAD motion, six miniature contacting potentiometers of type Variohm PZ12A were used. This product delivers accurate signals with high dynamics as well as low friction. To avoid supply errors, the ratio of signal to supply voltage was evaluated. Due to a high tolerance of the nominal resistance, calibration was done manually on a milling machine. The technical data of the linear motion position sensor type used are listed in Table B1.

Table B1 Data of the linear motion position sensor Variohm PZ12A

Supply voltage	4.95 V
Nominal travel	25 mm
Linearity error	$\leq$ 0.2 %offullscale
Nominal resistance	1 kΩ
Net weight	70 g
Ingress protection code	65

B2 Torque transducers

The torques on both dynos were measured with help of two digital contactless torque transducers of type HBM T12. Additionally to the torques, the transducers can also measure the corresponding rotational speed. The technical data of the digital torque tranducer type used are listed in Table B2.

Table B2 Data of the torque transducer HBM T12

Nominal torque	$6\ \mathrm{kNm}$
Output frequency	30–90 kHz
Nominal accuracy	±0.03 $\%offullscale$
Linearity error for 0–1 kNm	±0.006 $\%offullscale$

C Simulation parameters of the MBS reference model

Table C1 gives the main simulation parameters used for the measurement-adjusted MBS reference model of the ERAD of the Renault Twizy 80. For the mass, centre of gravity and inertia data, all bodies of the ERAD are considered, that is to say: housing, electric motor, shafts, gears, bearings, crown wheel, differential cage, etc.

Table C1 Simulation parameters of the measurement-adjusted MBS reference model of the ERAD of the Renault Twizy 80

Designation	*Symbol*	*Value*
Total mass	m	48.5 kg
Centre of gravity (COG) [a]	$[x; y; z]$	$[27.3; -194.6; -157.2]\ \mathrm{mm}$
Main diagonal inertia at COG [b]	$[I_{xx}; I_{yy}; I_{zz}]$	$[1.7977; 1.4454; 1.9592]\ \mathrm{kg \cdot m^2}$
Off-diagonal inertia at COG [c]	$[I_{xy}; I_{xz}; I_{yz}]$	$[0.2181; 0.0499; -0.0670]\ \mathrm{kg \cdot m^2}$
TRA definition point A [a]	$[x; y; z]$	$[123.8; -422.5; -255.4]\ \mathrm{mm}$
TRA orientation [d]	$[\alpha; \beta; \gamma]$	$[21.3; 6.4; -74.0]\ \mathrm{deg}$
Inertia about the TRA	I	0.4146 $\mathrm{kg \cdot m^2}$
Reduction gear ratio	i_1	3.222
Differential gear ratio	i_2	2.212
Rubber bushing location B_1 [a]	$[x; y; z]$	$[0.0; 0.0; 0.0]\ \mathrm{mm}$
Rubber bushing location B_2 [a]	$[x; y; z]$	$[0.0; -300.0; -280.0]\ \mathrm{mm}$
Rubber bushing location B_3 [a]	$[x; y; z]$	$[217.9; -461.7; -256.8]\ \mathrm{mm}$
Rubber bushing stiffnesses B_1		
•x direction	$k_{1\,x}$	$438\ \frac{\mathrm{N}}{\mathrm{mm}}$
•y direction	$k_{1\,y}$	$94\ \frac{\mathrm{N}}{\mathrm{mm}}$
•z direction	$k_{1\,z}$	$722\ \frac{\mathrm{N}}{\mathrm{mm}}$
Rubber bushing stiffnesses B_2		
•x direction	$k_{2\,x}$	$1186\ \frac{\mathrm{N}}{\mathrm{mm}}$
•y direction	$k_{2\,y}$	$227\ \frac{\mathrm{N}}{\mathrm{mm}}$
•z direction	$k_{2\,z}$	$525\ \frac{\mathrm{N}}{\mathrm{mm}}$

Table C1 Simulation parameters of the measurement-adjusted MBS reference model of the ERAD of the Renault Twizy 80 (continued)

Designation	*Symbol*	*Value*
Rubber bushing stiffnesses B_3		
•x direction	$k_{3\,x}$	$1929\ \frac{\mathrm{N}}{\mathrm{mm}}$
•y direction	$k_{3\,y}$	$1273\ \frac{\mathrm{N}}{\mathrm{mm}}$
•z direction	$k_{3\,z}$	$293\ \frac{\mathrm{N}}{\mathrm{mm}}$
Maximum motor torque	$T_{\mathrm{m\,Max}}$	57 Nm (to 2100 min^{-1})
Maximum motor rotational speed	$n_{\mathrm{m\,Max}}$	5800 min^{-1}

[a] Measured from bushing B_1; [b] Main diagonal elements of the corresponding tensor; [c] Off-diagonal elements of the corresponding tensor; [d] Cardan angles.

D Modes of the electric rear axle drive

The six modes of the elastically mounted Twizy ERAD were calculated numerically within Simpack on basis of the measurement-adjusted MBS reference model from Section 4.2, see Figure D1.

Figure D1 Modes of the elastically mounted Twizy ERAD

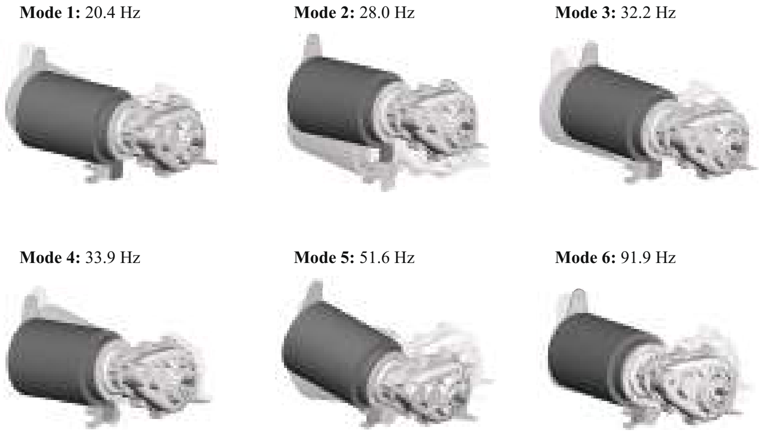

Mode 1: 20.4 Hz

Mode 2: 28.0 Hz

Mode 3: 32.2 Hz

Mode 4: 33.9 Hz

Mode 5: 51.6 Hz

Mode 6: 91.9 Hz